Carbon Structures Grown by Direct Current Microplasma: Diamonds, Single-Wall Nanotubes, and Graphene

Francesco Ghezzi,*[,†] Gabriele Cacciamani,[‡] Roberto Caniello,[†] Dana Cristina Toncu,[§] Federica Causa,[∥] David Dellasega,[†,⊥] Valeria Russo,[⊥] and Matteo Passoni[†,⊥]

[†]Istituto di Fisica del Plasma Piero Caldirola, Consiglio Nazionale delle Ricerche, via R. Cozzi 53, 20125 Milano, Italy

[‡]Dipartimento di Chimica e Chimica Industriale, Universita di Genova, Via Dodecaneso 31, 16146 Genova, Italy

[§]Department of Aerospace Engineering, Politehnica University from Bucharest, 1-7 Polizu, 01160 Bucharest, Romania

[∥]Associazione EURATOM-ENEA C. R. Frascati, via E. Fermi 45, 00044 Frascati, Roma, Italy

[⊥]Dipartimento di Energia, Politecnico di Milano, via Ponzio 34/3, 20133 Milano, Italy

INTRODUCTION

Chemical vapor deposition (CVD) and plasma assisted CVD have now been proven to be an effective deposition technique for a variety of carbon materials including diamond[1] and graphene.[2−4] Among the CVD techniques, the focus is on direct current microplasma technique (DCμP). This technique is based on the micro-hollow-cathode effect, which allows production of a high density plasma (up to 10^{16} cm^{-3}) and has the ability to start the discharge at relatively high pressures (close or equal to atmospheric pressure).[5] Importantly, the plasma presents a non-negligible fraction of electrons with high energy (>10 eV) allowing a variety of chemical reactions, including the formation of energetic radical precursors in CVD deposition methods. Thanks to these properties, DCμP has been successfully employed for various applications such as nanostructure synthesis,[6] semiconductor device post processing,[7] UV emission,[8] diamond,[9] and few-layer graphene deposition.[10]

However, thermodynamic and kinetic aspects of DCμP deposition technique have not yet been fully elucidated, particularly for diamond deposition. On the other hand an extensive analysis based on nonequilibrium nondissipative thermodynamic was formulated for the case of hot filament diamond deposition[11,12] to explain the apparent thermodynamics infringement occurring in plasma-based diamond CVD.

In this work the DCμP is presented as a simple deposition technique to obtain different carbon structures by varying the operating parameters (i.e., substrate temperature and working pressure). This paper is organized as follows: the DCμP technique and characterization of the deposited carbon structures by scanning electron microscopy (SEM) and micro-Raman spectroscopy are presented and discussed in the Experimental Section. The nonequilibrium, nondissipative method is introduced and applied to describe the experimental results in section the Thermodynamic Model section.

EXPERIMENTAL SECTION

The experimental apparatus used for deposition of carbon-based materials is presented in Figure 1a. The equipment includes vacuum system, plasma generating system, and gas supply system. The vacuum system consists of a ∼14 L stainless steel vacuum chamber evacuated by a primary rotary pump (Pfeiffer) and a turbomolecular pump (Varian V70), inline valves (VAT), feedback control valve (MKS 250), capacitance manometer (MKS 120), and high pressure ionization gauge (Balzers IMR 125). The core of the experimental setup is the

Received: February 10, 2014
Revised: October 2, 2014
Published: October 2, 2014

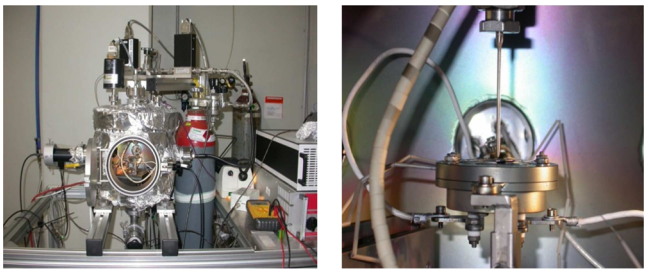

(a) (b)

Figure 1. Experimental equipment: plasma vacuum chamber (a) and microplasma jet setup (b).

in-house designed stainless-steel column with a 178 μm inner diameter capillary tube acting as the microhollow cathode allowing the gas inlet used to create the flow-stabilized microplasma jet, Figure 1b. The anode is a grounded furnace holding and heating the sample. Heating occurs via thermal radiation using a tungsten wire (100 μm, 4 Ω).

Two quartz windows are suitably positioned for both visual and instrumental inspection of the microplasma jet. The furnace and sample temperatures are monitored by two K-type thermocouples: the first is placed directly on the substrate while the second is at the furnace shield. The discharge is sustained by supplying a negative voltage to the capillary via a dedicated short-protected dc power supply (GERÄT EA-HV 9000−1k2−2000). The discharge current and voltage are read across a series (ballast) power resistor (20 kΩ, 50 W). The carbon source is methane gas mixed with hydrogen. The gas supply system consists of two mass flow controllers (MKS 1280) (100 sccm full scale for H_2 and 10 sccm for CH_4), a manual isolation valve (NUPRO SS4BK), pressure reducers, and gas cylinders. The volt−amperometric (V−I) characteristic of the discharge and the influence of the micro-hollow-cathode geometry on the quality of the deposition were reported elsewhere.[13] The substrate is a polycrystalline molybdenum foil (11 mm diameter, 50 um thickness; 99.9% purity, Goodfellow). The range of operating conditions for CH_4/H_2 plasma deposition used in this work is summarized in Table 1.

Table 1. Range of Operating Conditions Used for Sample Deposition

substrate	Mo
feed gas	H_2, CH_4
excitation source	microplasma dc discharge
substrate temperature	500−1150 °C
total pressure	0.3−200 Torr
deposition time	3 h
flux parameter	ΦH_2, sccm: 100
	Φ CH_4, sccm: 0.5
	$\Phi H_2/\Phi CH_4$: 5×10^{-3}
discharge parameters	supply voltage, V: 550−650
	plasma current, mA: 9−15

Before deposition, the substrate was sonicated with hexane and deionized water and placed under vacuum in the deposition chamber for several hours. A predischarge of pure H_2 was performed for 10 min before introducing CH_4 gas to clean the substrate and to avoid temperature transients. During the deposition the total pressure was kept constant via the feedback control valve and capacitance gauge.

SEM micrographs were taken using a ZEISS Supra System with an accelerating voltage of 5 kV. Raman spectroscopy was performed in the visible range with a Renishaw InVia micro Raman spectrometer using the Ar laser blue line (λ= 457 nm). The Raman laser power was kept below 1 mW to avoid damage or modifications to the samples.

EXPERIMENTAL RESULTS AND DISCUSSION

As shown in Table 2, it is possible to deposit different types of carbon films by appropriately selecting the deposition parameters (e.g., working pressure and substrate temperature). Nature and physical properties of the samples were determined by the combined SEM and Raman analysis. To exemplify the information obtained by this powerful combined analysis, the results obtained for three samples representative of three different carbon structures (graphite, few-layer graphene, single-wall nanotubes) are shown in Figure 2. The three films exhibit very different morphologies: compact coating, Figure 2a; wrinkled thin carbon film, Figure 2b; tangles of nanowires, Figure 2c. Further information is obtained from the corresponding Raman analysis of the samples (lower panels of Figure 2). The compact film in Figure 2a presents the well-known Raman spectrum of polycrystalline graphite, with sharp D and G lines and multicomponent second order peak (indicated as 2D).[14] On the other hand the Raman spectrum of the thin wrinkled carbon film of Figure 2b clearly shows the typical features of rotationally faulted few-layer graphene (FLG), with the single Lorentzian-shape second order peak (2D) being much more intense than the G peak.[3,10,15] Finally the bundle of nanowires observed in Figure 2c is revealed to be single-wall carbon nanotubes (CNTs), presenting a Raman spectrum with the expected features known as G^+, G^-, and radial breathing modes (RBMs).[16]

Of particular interest is to use DCμP to deposit crystalline sp^3 carbon or diamond films, extending preliminary results obtained with this technique.[10] To this end, the SEM images and Raman spectra obtained from four samples deposited at the same working pressure (200 Torr) and CH_4/H_2 ratio (5×10^{-3}), but with different substrate temperatures (between 800 and 1100 °C), are presented in Figure 3a. It can be observed that the morphology of the samples changes depending on the substrate temperature. At the lowest temperature (800 °C) the film presents an open assembly of nanometric particles (100−300 nm) arranged in a cauliflower morphology. At the nanoscale, crystalline features can be observed on the surface of the individual particles. With an increase in the substrate temperature (900 °C), the deposited film is continuous, and nanometric crystalline facets (300−500 nm) are visible. Above 1000 °C, the growth of a microcrystalline film takes place and different facet shapes (square/rectangular and triangular) can be appreciated. At higher temperatures (1100 °C), the morphology returns to be cauliflower but on a wider scale than that obtained at lower temperatures. These observations are in agreement with those reported in the literature, indicating that the morphology of a CVD deposited diamond film (well-faceted, presence of small facets and cauliflowers) is deeply influenced by the process parameters. Usually the formation of a cauliflower structure is related to the use of high CH_4/H_2 ratio regardless of the type of deposition source.[17,18] This type of structure is reported to appear when using low-energy sources or a strong accelerating bias perturbing diamond growth.[19] On the other hand, evidence of cauliflower structures

Table 2. Samples Deposited Varying Working Pressure and Substrate Temperature[a]

P (Torr)/T (°C)	500	600	700	800	900	905	970	1000	1020	1100	1150
0.3	nD										
5					CNT						
10		G									
42							MLG				
70			G	nD	D			FLG			
100	G	G	G	D							
200				D		D			D	D	FLG

[a]The attributed structure of the obtained carbon material is reported on the basis of Raman and SEM characterization (G = graphite, FLG = few-layer graphene, MLG = multilayer graphene, CNT = carbon nanotubes, nD = nanodiamond, D = diamond).

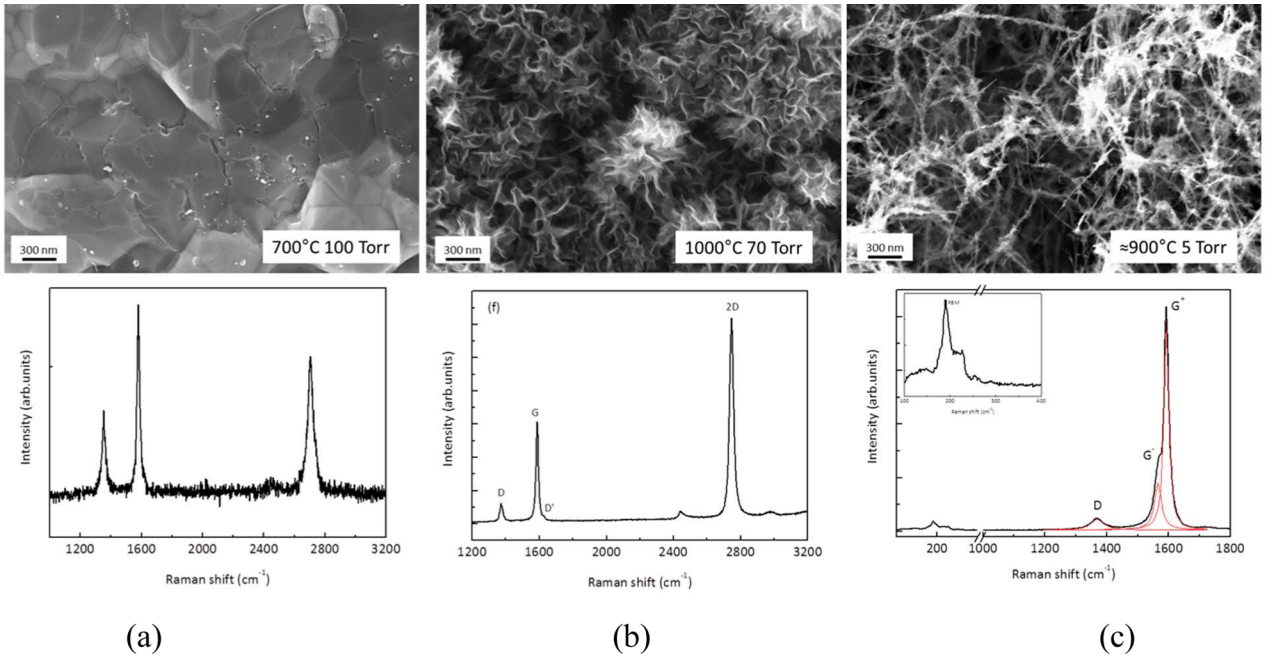

Figure 2. SEM micrographs and Raman spectra of carbon-based films deposited at different pressures and temperatures: (a) 700 °C, 100 Torr; (b) 1000 °C, 70 Torr; (c) 900 °C, 5 Torr.

in the first stages of microcrystalline diamond deposition has also been reported.[20]

The few published studies on the influence of substrate temperature on diamonds growth indicate that low temperatures lead to the deposition of cauliflower morphology[21] at a given pressure. From the results presented in Figure 2, it is noted that, at 200 Torr, higher substrate temperatures promote the growth of larger and more regular diamond grains, up to a certain temperature, after which cauliflower growth reappears, possibly due to the consequent higher hydrogen desorption rate that increases defect density in the structure.[21]

Despite these differences in morphology, the Raman spectra obtained from all four samples clearly show the signature of CVD diamond films.[22] This is characterized by a sharp peak at about 1332 cm^{-1}, related to the first order diamond line, superimposed to large bands (indicated by D and G on the spectra), due to the sp^2 carbon components always present in the bulk or at the grain boundaries of diamond films. The width of the diamond peak and the relative intensity between this peak and the contribution of the others nondiamond phases increase with increasing temperature, indicating a higher quality film. Further, the two features observed at about 1150 and 1520 cm^{-1} are assigned to the ν_1 and ν_3 peaks of *trans*-polyacetylene present at grain boundaries.[23]

The great advantage of the DCμP technique is that it enables the deposition of sp^3 carbon even at low temperature and low pressure, as shown by the SEM and Raman analysis of a film deposited in these conditions (500 °C, 0.3 Torr), Figure 3b. The deposition spot is constituted by micrometric aggregates, where crystalline features can be appreciated, a type of morphology related to nanodiamond deposition.[17] On the aggregate surface a dispersion of nanoparticles is visible. The corresponding Raman spectrum, right-hand side of Figure 3b, is typical of so-called nanodiamond or ultrananocrystalline diamond[23] with a small but broad (fwhm 35 cm^{-1}) diamond peak at about 1332 cm^{-1} and a prevalent signal from the nondiamond sp^2 phase, a mixture of amorphous carbon and olephinic molecules. This type of material is desirable for the valuable mechanical and electrochemical properties of the smaller grains.[23]

In conclusion, the DCμP technique can be readily used to deposit a variety of diamond and carbon-based structures by changing temperature and pressure, as demonstrated by the range of experimental results presented here. The theoretical basis at the core of the experimental observations reported here is presented in the next section.

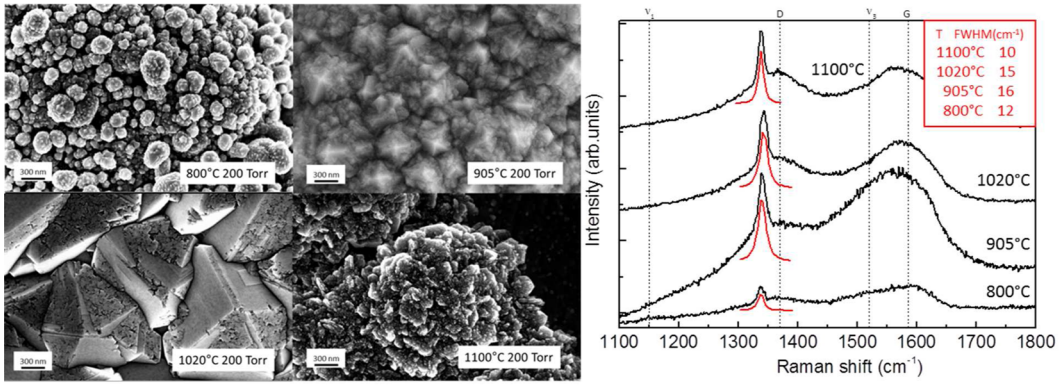

(a)

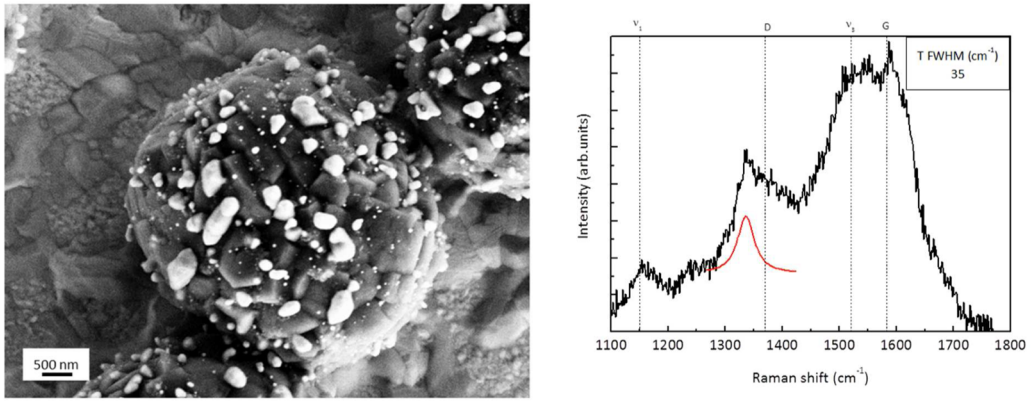

(b)

Figure 3. SEM and Raman analysis of diamond films deposited with dc microplasma: (a) P = 200 Torr and T = 800−1100 °C as indicated; (b) P = 0.3 Torr and T = 500 °C. The fwhm of the Lorentzian fitting of the diamond peak is reported in the inset.

THERMODYNAMIC MODEL

Reaction Mechanism for Diamond Formation in CVD.

Diamond deposition by CVD and plasma assisted CVD has been described using different reaction mechanisms, often including even hundreds of intervening reactions[24,25] and detailed computational analysis.[21,26] Piekarczyk's model[27−30] based on three reaction steps is here taken as the reference criterion to identify the best working conditions for diamond formation by DCμP technique. That model is simple and suitable to be used in a thermodynamic formulation, according to the approach introduced by Wang.[11]

Due to the strength of the carbon−hydrogen and carbon−carbon bonds, diamond deposition requires hydrogen displacement from the carbon surface and the generation of growth sites by hydrogen desorption. This requires an increased atomic hydrogen concentration in the gas phase to make the hydrogen-terminated surface more labile, and promote growth of the desired carbon structure.

Following[27−30] the reaction mechanism for diamond growth which at constant carbon surface temperature and total pressure consists of three cyclically recurring consecutive surface reactions: (1) Formation of unsaturated (i.e., containing sp^2 bonds) carbon−hydrogen clusters, $C_2H_2(2C_{Dia})$, occurs on a labile hydrogen-terminated surface of a diamond seed, $H(C_{Dia})$

$$2H(C_{Dia}) + 2C_{gas} \leftrightarrows C_2H_2(2C_{Dia}) \quad (1)$$

where C_{Dia} represents carbon atoms on the diamond surface and C_{gas} represents carbon dissolved in the gas phase. (2) Hydrogenation of the unsaturated clusters, i.e., conversion of the unsaturated clusters $C_2H_2(2C_{Dia})$ into saturated ones $C_2H_4(2C_{Dia})$ containing only sp^3 bonds, occurs by impact of superequilibrium atomic hydrogen, H^*_{gas}

$$C_2H_2(2C_{Dia}) + 2H^*_{gas} \leftrightarrows C_2H_4(2C_{Dia}) \quad (2)$$

where H^*_{gas} is atomic hydrogen at the energy and concentration expected when in thermal equilibrium with the other gas species, with the gas temperature (2000−4000 °C) being much higher than surface temperature (500−1200 °C). It is to be noted that the equilibrium concentration of atomic H in the gas phase increases by a factor 10^4 from 1000 to 2000 °C. Such atomic hydrogen is defined to be in a *superequilibrium* state at the surface temperature. (3) Coalescence of saturated clusters results in the formation of a new layer of sp^3 carbon with diamond structure (C_{Dia}), with simultaneous recreation of the hydrogen-terminated surface

$$C_2H_4(2C_{Dia}) \leftrightarrows 2C_{Dia} + 2H(C_{Dia}) + H_2 \quad (3)$$

where H_2 represents gaseous molecular hydrogen at the surface temperature.

The overall reaction obtained by combining the three above-mentioned steps contains only reactants of known thermodynamic properties:

$$C_{gas} + H^*_{gas} \leftrightarrows C_{Dia} + 0.5H_2 \quad (4)$$

dx.doi.org/10.1021/jp501440b | J. Phys. Chem. C 2014, 118, 24714−24722

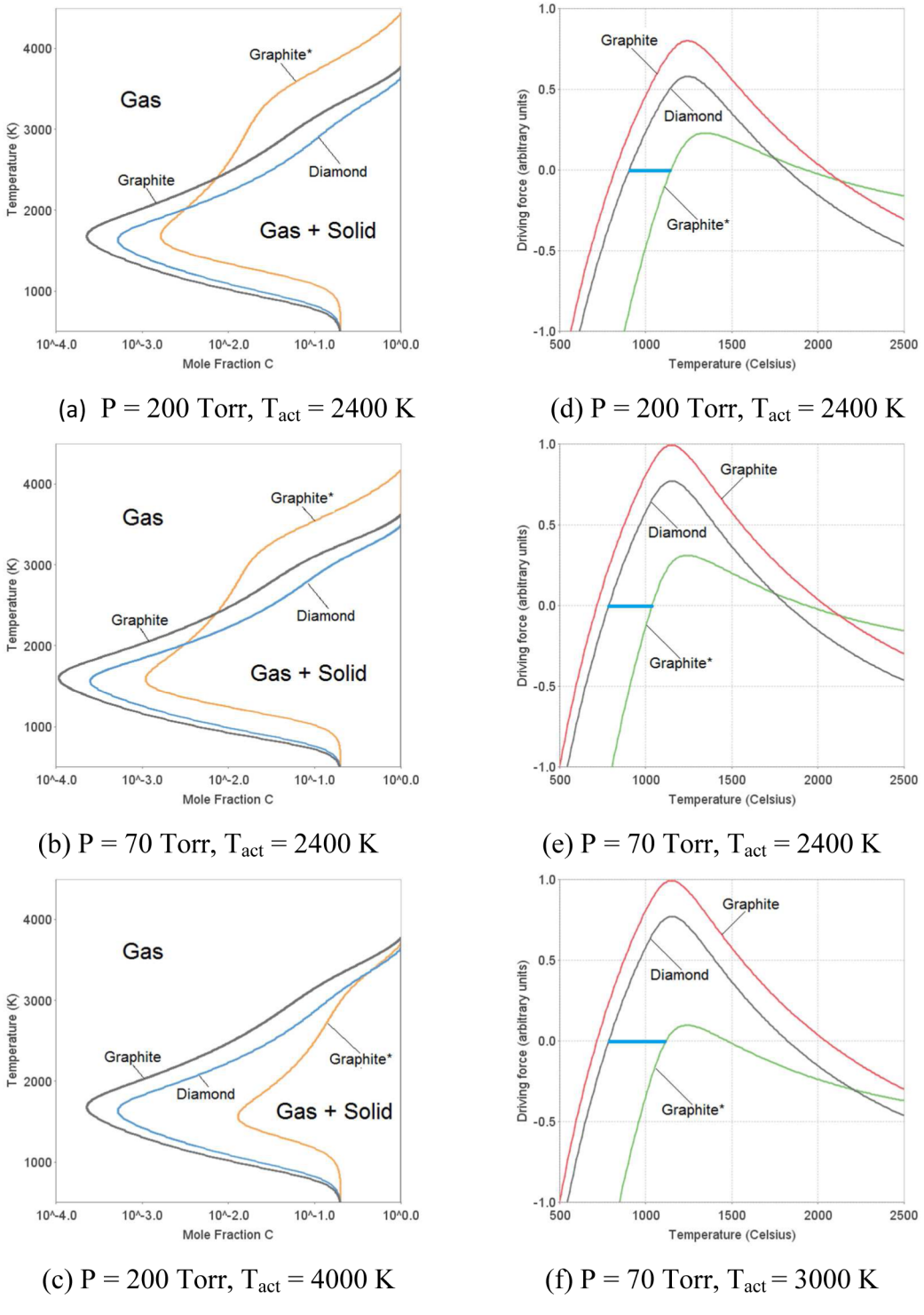

Figure 4. Left panels (a–c): Gas–solid equilibria in the isobaric C–H phase diagram. Diagrams are calculated independently for the three solid phases diamond (blue), regular (black), and activated graphite (orange), at the temperatures and pressures indicated. Right panels (d–f): Driving force for graphite (red), diamond (black), and graphite* (green) deposition calculated for 0.5% CH_4 concentration and the pressures and temperatures indicated. The blue segments show the temperature range favorable for diamond growth.

Equation 4 points out that superequilibrium atomic hydrogen can move the global reaction toward diamond formation. This equation is the core of the thermodynamic model described in the following section.

Thermodynamic Model. The above-mentioned reaction mechanism is a nonequilibrium process because it involves reactants at different temperatures. However, it is a stationary process because temperature and composition of each reactant remain constant during the process. A nonequilibrium stationary process is governed by the minimization of entropy production rather than minimization of the Gibbs free energy. However, if the minimum value of entropy production tends to zero, the entropy production minimization principle becomes equivalent to the Gibbs free energy minimization principle. This is the case for CVD diamond formation.[11,12,31] In this model the following assumptions are proposed: (1) An

adequate concentration (larger than the equilibrium concentration) of superequilibrium atomic hydrogen (H*) is present at the gas−solid interface. (2) The activation temperature, T_{act}, of superequilibrium atomic hydrogen is the temperature of the gas phase (i.e., plasma phase). (3) The surface carbon interacting with superequilibrium atomic hydrogen is represented by C^*_{gra} and referred to as "activated graphite".

In agreement with the above-mentioned reaction mechanism, eqs 2 and 3 can be rewritten as

$$C_{gra} \leftrightarrows C_{dia} \quad G_1 > 0,\ T = T_s,\ P \le 10^5\text{Pa} \tag{6}$$

$$2H^* \leftrightarrows H_2 \quad \Delta G_2 \ll 0,\ T_s \ll T_{act},\ P \le 10^5\text{Pa} \tag{7}$$

where C_{gra} is the surface carbon in sp^2 hybridization state (as in the graphite phase), T_s is the substrate temperature, ΔG_i is the Gibbs free energy, P is the total pressure. During the growth process the extra energy of the superequilibrium H* is supplied to the unsaturated carbon (sp^2 carbon, C_{gra}) and used to promote its saturation (sp^3 carbon, C_{dia}).

It is important to notice that the process described above is a simplification of the real process in which not only hydrogen but also more gaseous species (such as CH_3) are expected to take part, at least from a kinetic point of view.[26,32]

In the present thermodynamic model, eqs 6 and 7 are coupled by a coupling parameter χ (effectively the reaction rate ratio) to obtain

$$C_{gra} + \chi H^* \leftrightarrows \chi/2H_2 + C_{dia}$$
$$\Delta G_3 = \Delta G_1 + \chi \Delta G_2,\ T = T_s,\ P \le 10^5\text{Pa} \tag{8}$$

When χ is large enough ($\chi > \Delta G_1/\Delta G_2$), $\Delta G_3 < 0$, diamond formation is favored with respect to graphite. Under these circumstances also the already present graphite should convert to diamond.

To simplify the model, eq 8 is rearranged to obtain

$$C^*_{gra} \leftrightarrows C_{dia} \quad T_{act} >> T_s,\ P \le 10^5\text{Pa},\ \Delta G_{T,P} \le 0,$$
$$\Delta S \ge 0 \tag{9}$$

where $C^*_{gra} = C_{gra} + \chi(H^* - {}^1/_2H_2)$ is denoted as "activated graphite", with increased Gibbs energy (i.e., less stable) with respect to the original graphite. The Gibbs energy increase of C^*_{gra} is the Gibbs energy released by the superequilibrium atomic hydrogen H* when it forms equilibrium molecular hydrogen.

The overall process represented by eq 9 is suitable for a thermodynamic analysis, with the properties of all substances being available in literature.[33] The parameters which affect thermodynamic properties of activated graphite are (1) total pressure P, (2) substrate temperature T_s, (3) activation temperature T_{act}, (4) overall carbon concentration in the gas phase $x(C)$, and (5) coupling parameter χ. All but χ are operating parameters that can be controlled experimentally during the CVD process.

The coupling parameter has been chosen to be $\chi = 0.28$, as suggested by Wang.[11]

Phase relations between gas, diamond, and regular and activated graphite can be represented by classical phase diagrams: favorable conditions for diamond growth are those where diamond is more stable than activated graphite.

As an introduction to our analysis, a series of isobaric composition/temperature phase diagrams for the C−H system are presented in Figure 4a−c. In the graphs, gas−solid equilibria are calculated separately for diamond, regular graphite, and activated graphite. Then, each graph is the superposition of three different phase diagrams, each calculated independently considering only one of the three solid phases.

In the phase diagrams of Figure 4a−c each curve separates the region where only the gas phase is stable (on the left) from the area where some amount of solid is stable, in equilibrium with the gas. All the graphs in Figure 4a−c show that, as expected, regular graphite is more stable than diamond at all substrate temperatures, as demonstrated by the fact that the first curve for graphite is on the left side of the first curve for diamond. In other words the carbon concentration in the saturated gas is lower when in equilibrium with graphite than with other phases. However, when superequilibrium hydrogen is present, graphite is destabilized to graphite*. As a consequence there is a range of experimental conditions where diamond is more stable than graphite* and can exist in equilibrium with gas. In particular, it is noted that graphite and graphite* curves cross at $T = T_{act}$, where H* is in equilibrium with H_2 and consequently graphite and graphite* are also in equilibrium (i.e., $G(\text{graphite}, T_{act}) = G(\text{graphite*}, T_{act})$). With respect to Figure 4a, the results do not fundamentally change when reducing the pressure, as shown for example in Figure 4b, calculated for $P = 70$ Torr: a comparison with Figure 4a reveals that decreasing total pressure slightly decreases the C mole fraction in the gas in equilibrium with the solid phases. On the other hand, by increasing the activation temperature, the temperature range where diamond is stable extends to higher temperatures, Figure 4c.

The relative carbon chemical potential in diamond and regular and activated graphite may be regarded as the driving force for the phase formation, provided the gas phase behaves ideally.[31] The corresponding curves calculated with the model described above are presented in Figure 4d−f as a function of (substrate) temperature. From Figure 4d it is seen that diamond deposition is favored when the diamond driving force is positive while that of graphite* is negative (in the case considered here, 900−1145 °C). At higher temperatures, where both driving forces are positive, codeposition of diamond and graphite should occur. By decreasing the pressure, Figure 4e, the favorable temperature range shifts appreciably to lower values (in the case considered, the range is 780−1040 °C). A more significant effect is obtained by increasing the activation temperature, as shown in Figure 4f. An increased activation temperature destabilizes graphite*, and as a consequence, the temperature interval in which simultaneously the driving force of graphite* is negative and that of diamond is positive extends upward, but not downward (in the case considered here: 790 and 1120 °C). Moreover, the diamond driving force increases with respect to the activated graphite, and therefore, this should favor the kinetics for diamond deposition.

Application of the Model to Microplasma Deposition. To enable useful comparisons of model calculations with experimental results and to predict the experimental conditions which favor diamond growth with respect to other carbon structures in DCμP, it is useful to calculate phase relations in the C−H system as a function of the operating parameters adopted experimentally. In DCμP the high-density plasma has the fundamental role of producing highly energetic radicals, including H*, essential in the growth of good-quality diamond. Temperature and pressure have been taken as variable parameters, keeping constant all the others (χ, $\Phi CH_4/\Phi H_2$, T_{act}). While the methane concentration was set experimentally

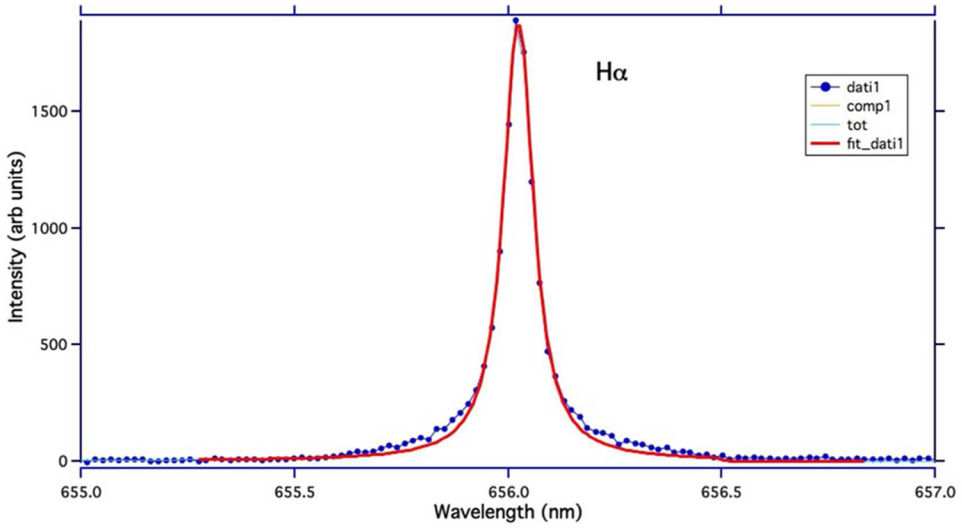

Figure 5. Deconvolution of the H_α line of excited neutral atomic hydrogen, with a Voigt profile (λ_0 = 6565 nm, $\Delta\lambda_G$ 0.025 0441 nm) obtained at P 200 Torr, $\Phi(H_2)$ = 100 sccm, $\Phi(CH_4)$ = 0.5 sccm, with the sample at ambient temperature, T_{sub} = 300 K.

to 0.5 mol %, the activation temperature should be determined experimentally. Atomic hydrogen temperature in the plasma was estimated by assessing the Doppler broadening of the H_α line[34] resulting in an average temperature of 2843 K, Figure 5. However, considering the difficulties associated with obtaining accurate and spatially resolved spectroscopic measurements in such a small volume of plasma (200 um diameter, 1 mm height), this parameter was chosen to be T_{act} = 2400 K, also according to literature.[35] The calculated phase diagrams and the experimental data obtained from all samples are presented in Figure 6. Regular graphite, which is more stable than both diamond and graphite*, but supposed not to be present when graphite* exits, has been omitted for clarity. The bell-shaped curves are the boundaries of the stability regions of the solid phases (either diamond or graphite*) with respect to the gas; the shaded area represents the conditions where diamond

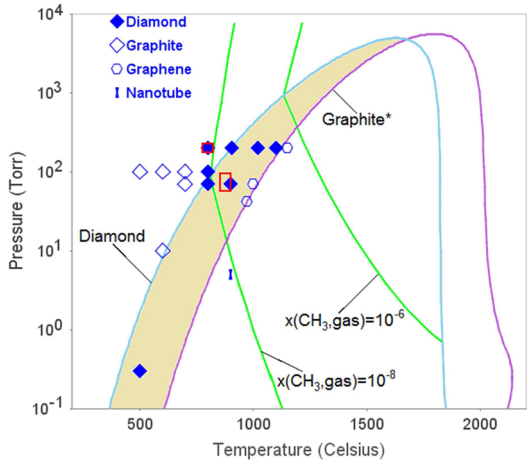

Figure 6. Pressure−temperature C−H phase diagram calculated for a $\Phi H_2/\Phi CH_4$ flux ratio of 5×10^{-3}, with T_{act} = 2400 K and χ = 0.28. Conditions favorable for diamond growth correspond to the shaded area. The symbols represent the experimental data obtained from the DCμP method described in the present work. The red squares represent experimental data obtained from refs 9 (200 Torr, 800 °C, $\Phi H_2/\Phi CH_4$ = 0.1−5%) and 36 (60−90 Torr, 850−900 °C, $\Phi H_2/\Phi CH_4$ = 0.5−2%).

growth takes place. The two green curves delimit the area where the mole fraction of the CH_3 species in the gas is between 10^{-6} and 10^{-8}, a favorable condition[36,37] to enhance diamond deposition kinetics. The experimental data of Table 2, represented by the symbols in Figure 6, fall in the corresponding areas of the phase diagram, demonstrating that the model can well interpret the wide range of structures obtained by the same deposition method.

Present model calculations are also in good agreement with results taken from the literature[9,38] represented by red squares in Figure 6 and described in the caption of the figure itself. A full comparison with other deposition methods is not always possible because of lack of experimental data in some of the work.[39,40]

In the light of the model it is now possible to complete the interpretation of the experimental SEM and Raman combined analysis, with the following observations: (1) For the particular pressure value of 200 Torr it was observed that both quality and dimensions of the experimentally obtained diamond films improve with increasing temperature. This is due to the increase of both the diamond driving force, as visible in Figure 4d, and of the CH_3 concentration in the gas (green curves in Figure 6). Actually CH_3 is the most abundant precursor for diamond formation at T = 1100 K and 0.5 mass % of CH_4, in agreement with the analysis by Zhang et al.[28] Moreover, results reported by Obraztsov et al.[38] (who obtained diamonds for T = 850−900 °C, P = 60−90 Torr, and CH_4 concentration of 0.5−2%) are in good agreement with the present model calculations. An interesting case is represented by the sample grown at 0.3 Torr and 500 °C where nanodiamonds are observed, Figure 6. These low pressure and temperature conditions are still in the diamond area, but outside the favored range of CH_3 concentration, giving rise to an sp^3 phase, but with nanometric grains. (2) By choosing parameters outside the diamond area, different carbon structures have been deposited, usually with a prevalence of the sp^2 phase. Graphite was obtained repeatedly operating to the left of the diamond stability curve, as expected. This means that in those experimental conditions no activated graphite is present and regular graphite is favored with respect to diamond. (3) Using growth conditions to the right of the diamond area, where graphite* is more stable than diamond,

more exotic forms of sp^2 carbon are preferred, such as few layer graphene and nanotubes. It is expected that, in these conditions, nucleated graphite is effectively etched by atomic hydrogen from the plasma, thus favoring the formation of structures composed by few graphitic layers, such as FLG, MLG, and CNTs.

CONCLUSIONS

Samples encompassing a wide range of chemical and physical parameters have been deposited using DCμP. By appropriately selecting the deposition parameters, carbon-based materials ranging from graphene and nanotubes to diamond can be obtained, demonstrating the versatility of this cost-effective deposition technique. SEM and Raman were used for the characterization of the samples.

As far as diamond growth is concerned, the best results were obtained with a T_s of about 1000 °C and pressure of 200 Torr resulting in the deposition of a microcrystalline diamond film. Above and below 1000 °C the quality of the diamonds does not change appreciably, but they grow in the so-called "cauliflower" fashion. T_s outside the range 800−1000 °C favors the deposition of graphitic phases, graphite, or few layer graphene, while decreasing the pressure carbon nanotube as well as nanodiamond are observed.

In addition, a thermodynamic model based on the literature was developed and adapted to the DCμP deposition technique to interpret the wealth of experimental data, obtaining a coherent view on the deposition technique based on the role of superequilibrium monatomic hydrogen and activated graphite. Setting the coupling parameter to 0.28 and the T_{act} to 2400 °C the model is able to predict the formation of either diamonds or graphitic phases as a function of the T_s and P as operating parameters.

Further experiments supported by the application of the same model to different CH_4 concentrations in the gas phase are foreseen.

AUTHOR INFORMATION

Corresponding Author

*E-mail: ghezzi@ifp.cnr.it. Phone: +390266173209.

Notes

The authors declare no competing financial interest.

REFERENCES

(1) Sung, J. C.; Lin, J. *Diamond Nanotechnology Syntheses and Applications*; Pan Stanford Publishing Pte. Ltd.: Singapore, 2010; pp 18−21.

(2) Novoselov, K. S.; Falko, V. I.; Colombo, L.; Gellert, P. R.; Schwab, M. G.; Kim, K. A Roadmap for Graphene. *Nature* **2012**, *490*, 192−200.

(3) Reina, A.; Jia, X.; Son, H. J.; Nezich, D.; Hyungbin, S.; Bulovic, V.; Dresselhaus, M. S.; Kong, J. Large Area, Few-Layer Graphene Films on Arbitrary Substrates by Chemical Vapor Deposition. *Nano Lett.* **2009**, *9*, 30−35.

(4) Heiman, A.; Gouzman, I.; Christiansen, S. H.; Strunk, H. P.; Hoffman, A. Nano-diamonds Films Deposited by Direct Current Glow Discharge Assisted Chemical Vapor Deposition. *Diamond Relat. Mater.* **2000**, *9*, 866−871.

(5) Schoenbach, K. H.; Moselhy, M.; Sci, W.; Bentley, R. Microhollow Cathode Discharges. *J. Vac. Sci. Technol., A* **2003**, *21*, 1260−1265.

(6) Mariotti, D.; Mohan Sankaran, R. Microplasmas for Nanomaterials Synthesis. *J. Phys. D: Appl. Phys.* **2010**, *43* (323001), 1−21.

(7) Choi, J.; Matsuo, K.; Yoshida, H.; Namihira, T.; Katsuki, S.; Akiyama, H. Characteristics of a DC-Driven Atmospheric Pressure Microplasma Jet. *Jpn. J. Appl. Phys.* **2008**, *47*, 6459−6463.

(8) Boeuf, J. P.; Pitchford, L. C.; Schoenbach, K. H. Predicted Properties of Microhollow Cathode Discharges in Xenon. *Appl. Phys. Lett.* **2005**, *86* (071501), 1−3.

(9) Sankaran, M. R.; Giapis, K. P. Hollow Cathode Sustained Plasma Microjets: Characterization and Application to Diamond Deposition. *J. Appl. Phys.* **2002**, *92*, 2406−2411.

(10) Passoni, M.; Russo, V.; Dellasega, D.; Causa, F.; Ghezzi, F.; Wolverson, D.; Bottani, C. E. Raman Spectroscopy of Nonstacked Graphene Flakes Produced by Plasma Microjet Deposition. *J. Raman Spectrosc.* **2012**, *43*, 884−888.

(11) Wang, J. T. *Nonequilibrium Nondissipative Thermodynamics With Application to Low-Pressure Diamond Synthesis*; Springer-Verlag: New York, 2002; pp 99−137.

(12) Wang, J. T.; Wan, Y.-Z.; Liu, Z.-J.; Wang, H.; Wei Zhang, D.; Huang, Z.-Q. Phase Diagrams for Activated CVD Diamond Growth. *Mater. Lett.* **1998**, *33*, 1 l−3 14.

(13) Causa, F.; Ghezzi, F.; Dellasega, D.; Caniello, R.; Grosso, G. Analysis of Cathode Geometry to Minimize Cathode Erosion in Direct Current Microplasma Jet. *J. Appl. Phys.* **2012**, *112*, 123302−1−123302−7.

(14) Ferrari, A. C.; Meyer, J. C.; Scardaci, V.; Casiraghi, C.; Lazzeri, M.; Mauri, F.; Piscanec, S.; Jiang, D.; Novoselov, K. S.; Roth, S.; Geim, A. K. Raman Spectrum of Graphene and Graphene Layers. *Phys. Rev. Lett.* **2006**, *97*, 1874011−1874014.

(15) Li, X.; Cai, W.; An, J.; Kim, S.; Nah, J.; Yang, D.; Piner, R. Large-Area Synthesis of High-Quality and Uniform Graphene Films on Copper Foils. *Science* **2009**, *324*, 1312−1314.

(16) Jorio, A.; Saito, R.; Dresselhaus, G.; Dresselhaus, M. S. Determination of Nanotubes Properties by Raman Spectroscopy. *Phil. Trans. R. Soc., A* **2004**, *362*, 2311−2336.

(17) Chen, W.; Lu, X.; Yang, Q.; Xiao, C.; Sammynaiken, R.; Maley, J.; Hirose, A. Effects of Gas Flow Rate on Diamond Deposition in a Microwave Plasma Reactor. *Thin Solid Films* **2006**, *515*, 1970−1975.

(18) Jeon, I.-D.; Park, C. J.; Kim, D.-Y.; Hwang, N. M. Effect of Methane Concentration on Size of Charged Clusters in the Hot Filament Diamond CVD Process. *J. Cryst. Growth* **2001**, *223*, 6−14.

(19) Kadlecikova, M.; Vojs, M.; Breza, J.; Vesely, M.; Frgala, Z.; Michalka, M.; Matejkova, J.; Vojackova, A.; Danis, T.; Marton, M. Microwave and Hot Filament Chemical Vapour Deposition of Diamond Multilayers on Si and WC−Co Substrates. *Microelectron. J.* **2007**, *38*, 20−23.

(20) Lai, W. C.; Wu, Y.; Chang, H.; Lee, Y. Differing Morphologies of Textured Diamond Films with Electrical Properties Made with Microwave Plasma Chemical Vapor Deposition. *Appl. Surf. Sci.* **2010**, *257*, 1729−1735.

(21) Haubner, R.; Lux, B. Deposition of Ballas Diamond and Nano-Crystalline Diamond. *Int. J. Refract. Met. Hard Mater.* **2002**, *20*, 93−100.

(22) Prawer, S.; Nemanich, R. J. Raman Spectroscopy of Diamond and Doped Diamond. *Phil. Trans. R. Soc., A* **2004**, *362*, 2537−2565.

(23) Ferrari, A. C.; Robertson, J. Raman Spectroscopy of Amorphous, Nanostructured, Diamond−Like Carbon, and Nano-diamond. *Phil. Trans. R. Soc., A* **2004**, *362*, 2477−2512.

(24) Coltrin, M. E.; Dandy, D. S. Analysis of Diamond Growth in Subatmospheric DC Plasma Gun Reactors. *J. Appl. Phys.* **1993**, *74*, 5803−5820.

(25) Kondoh, E.; Ohta, T.; Mitomo, T.; Ohtsuka, K. Experimental and Calculational Study on Diamond Growth by an Advanced Hot Filament Chemical Vapor Deposition Method. *J. Appl. Phys.* **1992**, *72*, 705−711.

(26) May, P. W.; Mankelevich, Yu. A Experiment ad Modeling of the Deposition of Ultrananocrystalline Diamond Films Using Hot Filament Chemical Vapour Deposition and $Ar/CH_4/H_2$ Gas Mixtures: A Generalized Mechanism for Ultrananocrystalline Diamond Growth. J. *Appl. Phys.* **2006**, *100*, 024301−024309.

(27) Piekarczyk, W. Crystal Growth of CVD Diamond and Some of its Peculiarities. *Cryst. Res. Technol.* **1999**, *34*, 553−563.
(28) Piekarczyk, W. Diamond-Vapour Interface and Processes Proceeding on it During Growth of Diamond Crystal I. Diamond (111) Face. *J. Cryst. Growth* **1992**, *119*, 345−362.
(29) Piekarczyk, W.; Prawer, S. Role of Atomic Hydrogen in Preventing Surface Reconstruction and sp^2 Bond Formation During Chemical Vapour Deposition of Diamond. *Diamond Relat. Mater.* **1993**, *2*, 41−47.
(30) Piekarczyk, W.; Prawer, S. Diamond-Vapour Interface and Processes Proceeding on it During Growth of Diamond Crystals II. Diamond (011) Face. *J. Cryst. Growth* **1994**, *135*, 172−182.
(31) Wei Zhang, D.; Wan, Y.-Z.; Liu, Z.-J.; Wang, J. T. Driving Force for Diamond Deposition in the Activated Gas Phase Under Low Pressure. *J. Mater. Sci. Lett.* **1997**, *16*, 1349−1351.
(32) Zhang, J.-Y.; Wang, P.-F.; Ding, S.-I.; Wei Zhang, D.; Wang, J. T.; Liu, Z.-J. Thermodynamics Analyses of the Effect of CH_3 and C_2H_2 on Morphology of CVD Diamond. *Thin Solid Films* **2000**, *368*, 266−268.
(33) JANAF Thermochemical Tables NSRDS-NBS 37.
(34) Penache, C.; Miclea, M.; Bräuning-Demian, A.; Hohn, O.; Schössler, S.; Jahnke, T.; Niemax, K.; Schmidt-Ḧocking, H. Characterization of a High-PressureMicrodischarge Using Diode Laser Atomic Absorption Spectroscopy. *Plasma Sources Sci. Technol.* **2002**, *11*, 476−483.
(35) Luque, J.; Juchmann, W.; Brinkman, E. A.; Jeffriesc, J. B. Excited State Density Distributions of H, C, C2, and CH by Spatially Resolved Optical Emission in a Diamond Depositing DC-Arcjet Reactor. *J. Vac. Sci. Technol., A* **1998**, *16.2*, 397−408.
(36) Regel, L. L.; Wilcox, W. R. Diamond Film Deposition by Chemical Vapour Transport. *Acta Astronaut.* **2001**, *48*, 129−144.
(37) Hsu, W. L. Mole Fractions of H, CH_3, and Other Species During Filament-Assisted Diamond Growth. *Appl. Phys. Lett.* **1991**, *59*, 1427−1429.
(38) Obraztsov, A. N.; Zolotukhin, A. A.; Ustinov, A. O.; Volkov, A. P.; Svirk, Yu.; Jefimovs, K. DC Discharge Plasma Studies for Nanostructured Carbon CVD. *Diamond Relat. Mater.* **2003**, *12*, 917−920.
(39) Hsu, W. L. Gas-Phase Kinetics During Microwave Plasma-Assisted Diamond Deposition: Is the Hydrocarbon Product Distribution Dictated by Neutral-Neutral Interactions? *J. Appl. Phys.* **1992**, *72*, 3102−3109.
(40) Reeve, S. V.; Weimer, W. A. Optimizing the Gas Phase Chemistry in a DC Arcjet Diamond Chemical Vapour Deposition Reactor. *Thin Solid Films* **1994**, *253*, 103−108.